Full length article

Digital twin for directional solidification of a single-crystal turbine blade

Haijie Zhang [a], Xiaoshan Liu [b,c], Dexin Ma [b,c], Min Song [b], Andreas Ludwig [a], Abdellah Kharicha [a], Menghuai Wu [a,*]

[a] *Chair for Simulation and Modelling of Metallurgy Processes, Department of Metallurgy, University of Leoben, A-8700 Leoben, Austria*
[b] *State Key Laboratory of Powder Metallurgy, Central South University, Changsha 410083, China*
[c] *Wedge Central South Research Institute, Shenzhen 518045, China*

ABSTRACT

Single-crystal superalloy turbine blades (TBs) fabricated using directional solidification are key components of aeroengines and gas turbines. Owing to thermal–solutal convection during solidification, such components are susceptible to flow-induced defects such as freckles and/or eutectic accumulation. The formation mechanisms of the above defects are well understood, but reliable theories or empirical laws are unavailable to guide the engineering production process as the thermal–solutal convection is sensitive to the alloy, Bridgeman furnace design, shape and internal structure of the TB, withdrawal parameters, etc. This study proposes a novel method to 'digitally twin' the directional solidification of the TB, i.e. to utilise a physically based numerical model to quantitatively simulate the solidification process, including freckle formation and eutectic accumulation. It includes two simulations: one for the global thermal field in the Bridgeman furnace, including the casting system, and the other for the flow and solidification within the casting component. The former is modelled using Pro-CAST, the latter is modelled using a volume-average-based multiphase solidification model, and both are coupled. To verify the digital twin concept, an actual industrial TB with slight geometrical modification (removal of the fins while maintaining the inner surface profile) was cast in a Bridgman furnace, and the as-solidified TB was inspected for freckles. An excellent agreement between the simulation and experimental results was obtained. Typically, an actual TB features a complex inner structure (fins) that connects the front and back blades with an average wall thickness of 1.5 mm. A fresh simulation was performed for the TB with inner fins. It was observed that the inner fins of the TB along with other process conditions, such as the shadowing effect of the furnace, play an important role in freckle formation. This study demonstrates the necessity of the digital twin in future TB production.

1. Introduction

Single-crystal turbine blades (TBs) of Ni-based superalloys fabricated using directional solidification (DS) have been widely employed in aeroengines and industrial gas turbines because of their high strength, microstructural stability, and corrosion resistance at extreme temperatures [1,2]. The formation of freckles [3], which are generally aligned parallel to the direction of gravity and appear as a trail of equiaxed grains accompanied by local enrichment of eutectics, is a significant issue encountered during the DS of TB. Another problem is the accumulation of eutectics in some upper sections (e.g. shroud) of the TBs [4]. Such defects cannot be eliminated by heat treatment, leading to a high scrap rate.

Numerous experimental studies on the freckle formation mechanism

have been performed using industrial superalloys [2–6] or model alloys such as Pb–Sn, Pb–Sb [7], and $NH_4Cl–H_2O$ [8]. It is well known that thermo–solutal convection resulting from the density inversion of the melt in the mushy zone is the primary source of freckle formation. In the event of an upward DS, the temperature gradient results in a negative density gradient (i.e. $d\rho/dz < 0$) owing to thermal expansion, whereas the enrichment of the light solute in the mushy zone results in a positive density gradient (i.e. $d\rho/dz > 0$) [8]. When the latter effect overwhelms the former, the solute-enriched liquid tends to rise, and some plumes nucleate at the solidification front. A long or short segregation channel is formed below each plume beneath the solidification front. The solute-enriched interdendritic liquid was sucked into the segregation channel and then transported into the bulk region by the plume. The potential remelting of the roots of high-order side arms of dendrites

---

leads to dendrite fragmentation [9], resulting in the formation of misoriented stray/spurious grains in the segregation channel, i.e. freckles [3,10]. Process conditions with a high cooling rate and high temperature gradient were found to be favourable for suppressing freckles [3,11,12]; however, this simple rule did not apply to all castings [13]. Some studies have suggested utilising the Rayleigh number (*Ra*) to evaluate the potential of freckle formation [5,7,11]. Again, this *Ra* criterion is rarely applicable to actual TBs owing to the complexity of the TBs' shape and inner structure, which renders the flow patterns in such castings unpredictable. Recently, Ma et al. performed systematic experiments and proposed several geometrical effects of TB on the freckling tendency, including the 'edge-effect' [14,15], 'shadow effect' [14, 15], 'step effect' effect [14], 'curvature effect' [16], and 'crystal orientation effect' [17]. However, their application to actual TB production processes remains challenging. For example, when a particular area of a TB encounters two or more of the aforementioned conflicting 'effects', it is impossible to determine which one would prevail.

Numerical modelling appears to be the most reliable approach for predicting freckle formation. Some solidification models [18–20] that directly consider the dendrite morphology at the microstructure scale provide an excellent explanation for the onset of freckles. However, the computational costs of these models are extremely high. The calculations must be performed for a small portion of the TB with an over-simplified geometry. Additionally, such sophisticated models cannot couple the detailed effects of the global thermal field in the Bridgeman furnace (radiation, shadowing effect). Owing to these limitations, these models are unsuitable for the engineering-scale calculation of industrial TB. Recent studies indicate that the volume-average (VA)-based solidification model remains the most promising method for such applications [21–23]. The microscopic phenomena are volume-averaged and coupled with macroscopic multiphase transport processes. The capability and calculation efficiency of such models for predicting the onset and subsequent development of freckles have been proven [21,22,24–26].

Several TBs are cast in a cluster and assembled around a central rod in the commercial process [6,27]. Owing to the shadowing effect in the Bridgeman furnace, the blade facing the inducing wall can be approximately 20 K hotter than that facing the central rod [14]. According to experiments, the shadow side of the blade is freckle-prone, whereas the heating side is freckle-free [13,14,28]. The design of the ceramic core for producing the inner profile of the TB further complicates both the thermal and flow fields within the TB during solidification [29]. However, the effect of the designed inner structure of the TB, such as fins (for the TB cooling system during its service), on freckle formation is unknown. To realise a purported digital twin of the engineering production process of TBs based on DS in an industry furnace, a quantitative simulation tool that can 'reproduce' the actual TB solidification process is necessary. It involves the calculation of the global thermal field in the Bridgeman furnace, including the casting system of TBs, multiphase fluid flow and mass transfer, solidification kinetics in the casting, the subsequent formation of the as-cast structure, and potential freckles, etc. To the best of our knowledge, no such tool is currently available.

In this study, a novel method to 'digitally twin' the DS process of TBs is proposed. The solidification process, including the freckle formation and eutectic accumulation, can be quantitatively simulated using a physically based numerical approach. It involves two simulations: one for the global thermal field in the Bridgeman furnace, which includes the casting system, and another for the flow and solidification inside the casing component. The former is created using ProCAST, whereas the latter is based on a VA-based multiphase solidification model, and both are coupled. To demonstrate the digital twin concept, an actual TB of the superalloy was cast in a Bridgman furnace, and inspected for freckles after solidification.

2. Engineering DS process of TBs and experiment design

During the engineering production of TBs via the DS process, a cluster of TBs is simultaneously cast in a Bridgman furnace. As depicted schematically in Fig. 1(a), a baffle separated the heating zone (upper part) from the cooling zone (lower part). The ceramic shell mould produced by the normal investment casting process was placed on a copper-chill base. A ceramic core was positioned within the mould to fabricate the inner surface profile of the TB. Before pouring, the shell mould was preheated to 1773 K (1500°C). The DS of the TBs was triggered by downwardly withdrawing the shell mould at a constant velocity. Because of the intense cooling of the chill plate, solidification initiated from the starter block at the lower end. Only one grain grew into the airfoil portion of the TB after the spiral grain selector.

In the current study, a unique experiment is designed to validate/verify the 'digital twin' concept for the DS process of TBs. The furnace, experimental parameters, and alloy used conformed to industry production conditions. However, a few adaptations are made to the TB to offer a freckle-prone condition: a low withdrawal rate (1.5 mm/min) is considered; the inner complex structure (known as fins or ribs) of the TB is eliminated, i.e. only one ceramic core is employed to produce the inner surface profile. The layout of the 1/12 scale furnace, including the casting system, which was designed for the late digital twin simulation, is depicted in Fig. 1(b)1(c). Two TBs were assembled in parallel on the chill plate with their concave side (pressure side) facing the inducting wall. This configuration (double TBs) favouring freckle formation is also inconsistent with production conditions. After the solidification process, the TB was taken from the ceramic shell mould, the riser and grain selector were mechanically removed, and the TB was sand-blasted. Finally, macroetching and metallographic examinations were performed to examine the as-solidified structure and freckles. The essential dimensions of TB are depicted in Fig. 1(d). Information regarding the inner and outer surface profiles of the TB is omitted for commercial reasons. A third-generation superalloy was utilised, and its composition is listed in Table 1.

Only one TB, as indicated by 'B' in Fig. 1(c), was analysed. After careful inspection, freckles are found only on the convex side (Fig. 2(a)), whereas the concave side is freckle-free (Fig. 2(b)). The freckle trials (I–IV) are depicted in Fig. 2(c). At the bottom of the TB, no freckles were detected, but two segregation channels (marked by orange lines) were found. All four freckles were detected below the platform on the airfoil. The light colour in the freckles indicates the presence of tiny stray grains. Freckle-II propagated for a brief distance before disappearing from the blade surface. Some stray grains in Freckle-II subsequently evolved into coarse misoriented dendrites, also known as silver defects [30]. Freckles that grew from below disappeared from the surface as they approached the platform. Right on the platform, no freckles are observed. Above the platform, the cross-section of the blade first contracts, then expands, and then contracts again. Correspondingly, freckles appear, then gradually disappear when the cross-section expands and then reappear. Notably, similar to previous studies [14], the freckles are not observed immediately after cross-section expansion, but rather after a short incubation period.

3. Digital twin method

The digital twin of the DS process of the TB in a Bridgeman furnace is realised in two steps. The first step was to calculate the global thermal field in the Bridgeman furnace, including the casting system, followed by the flow and solidification inside the TB. The former was created using ProCAST, and the latter was created using a VA-based multiphase solidification model. The cooling history of the temperature distribution (cooling curves) on the TB surface, as calculated using ProCAST, was transferred and interpolated into the VA-based solidification model as the thermal boundary conditions.
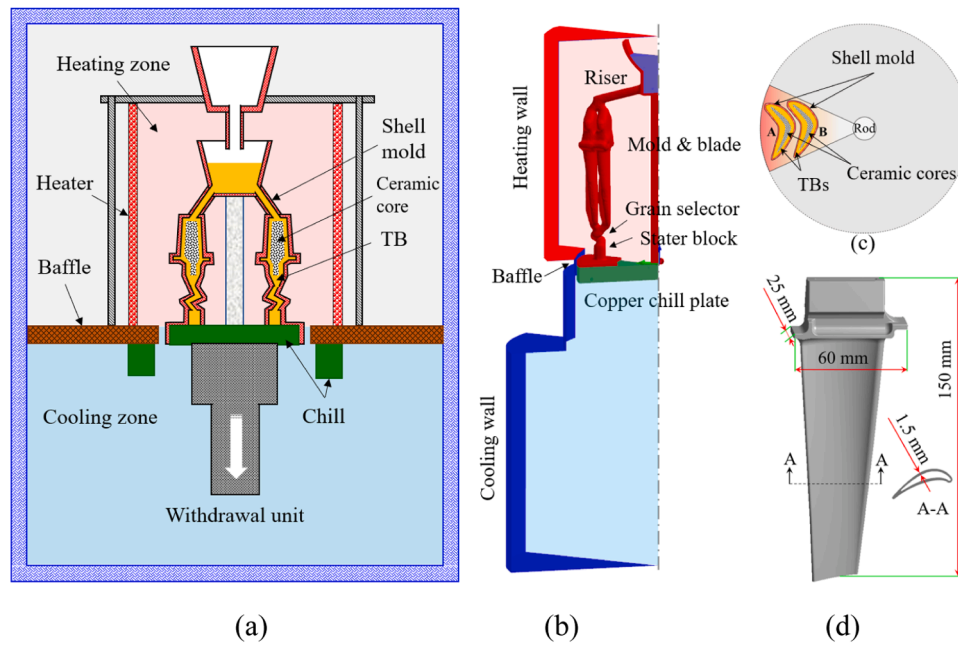
Fig. 1. (a) Configuration of the Bridgman furnace and casting system. (b) Layout of 1/12 furnace and the casting system. (c) The assembly of the two TBs around the central rod. (d) The key dimensions of the TB.

Table 1
The main composition of the considered superalloy.

Elements	Ni	Ta	Cr	Al	Co	W	Re	Ti	Mo
Content (wt.%)	-	8.07	3.39	5.69	5.97	6.52	4.89	0.15	0.41
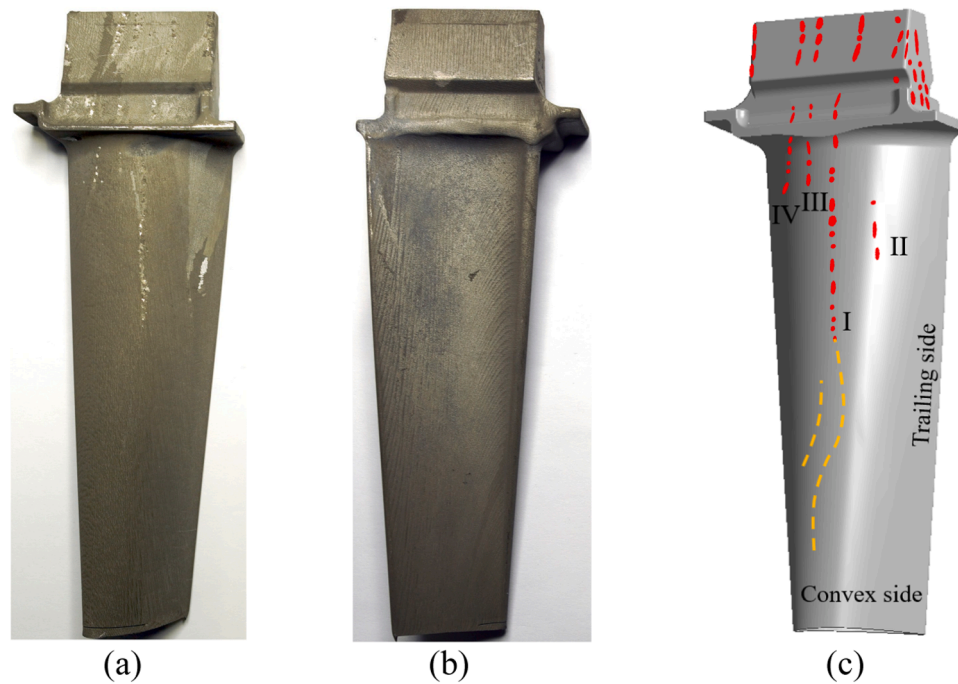
Fig. 2. As-cast TB and indicated freckles. Macrostructure on the convex side (a) and on the concave side (b). (c) Schematic display of the freckles on the TB. The red lines denote the freckles and the orange lines indicate segregation channles.
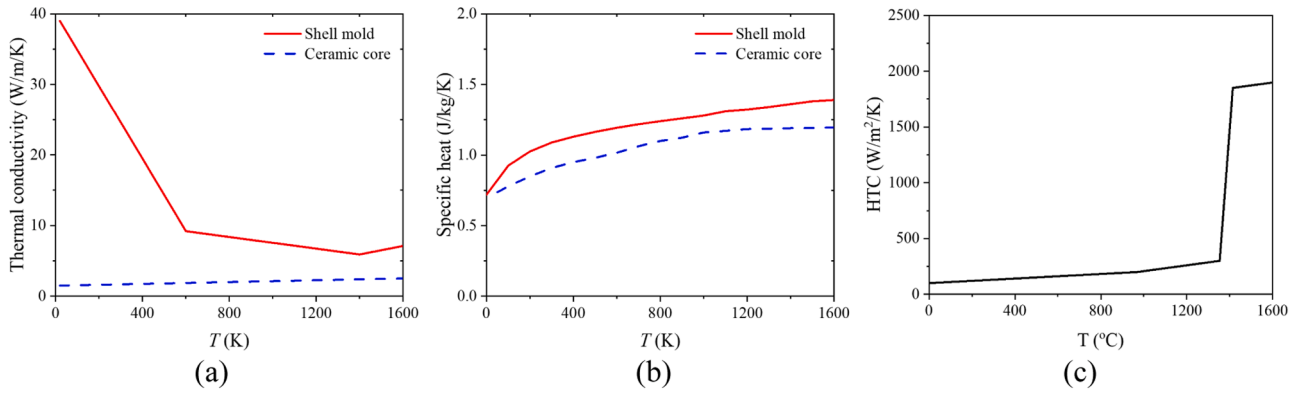
Fig. 3. Temperature-dependent properties and heat transfer parameters used for the thermal calculation: (a) Thermal conductivities of the shell mold and ceramic core; (b) Specific heat of the shell mold and ceramic core; (c) HTC (heat transfer coefficient) between superalloy with shell mold and ceramic core.

3.1. Calculation of the global thermal field in the Bridgeman furnace (ProCAST)

The full-scale geometry of the Bridgman furnace was constructed. As depicted in Fig. 1(b), only 1/12 of the furnace occupied by one pair of TBs was considered for the digital twin. The commercial software Pro-CAST was utilised to simulate the thermal field in the furnace, casting mould, and TB body. The TBs, ceramic core, mould, and chill plate were built using a 3D mesh. The withdrawing process of the mould and casting was achieved via raising the furnace. The simulation commenced with a mould completely filled by a liquid alloy at a uniform temperature, ignoring the mould filling process. Energy (enthalpy) conservation is solved in the ceramic core, superalloy, and shell mould, but only latent heat due to solidification of the superalloy is treated with an equivalent specific heat method.

$$\rho \frac{\partial h}{\partial t} = \nabla \cdot (k \nabla \cdot T), \tag{1}$$

with $h = \int_{T_{ref}}^{T} c_p^{equivalent} dT + h_{ref}$, where ρ and k are the density and thermal conductivity of the involved materials, h is the enthalpy, h_{ref} is the enthalpy at the reference temperature T_{ref}; $c_p^{equivalent}$ is the equivalent specific heat, for which an additional part due to solidification-induced latent heat in the solidification interval is added to the sensible heat capacity c_p, that is, $c_p^{equivalent} = c_p - \Delta h_f \partial f_s / \partial T$, where the solid volume fraction f_s is assumed to be a function of T based on the Gulliver–Scheil model, and Δh_f is the latent heat of fusion. For the mould and core materials, $c_p^{equivalent} = c_p$.

Radiation from the inducting wall of the furnace and the outer surface of the shell mould yield

$$Q_R = \sigma \varepsilon \left(T_w^4 - T_m^4 \right), \tag{2}$$

where σ is the Stefan–Boltzmann constant, ε is the emissivity, T_m is the mould surface temperature, and T_w is the inducting wall temperature. The radiation module of ProCAST accounted for the effects of reflection, obstruction, and shadowing by calculating the view factors. A theoretical introduction to this issue can be found in the literature [31,32]. The properties and parameters used for the ProCAST simulation are listed in Table 2.

3.2. Volume-average based solidification model

Flow and solidification were simulated using a VA-based multiphase solidification model. The model has been described in detail in previous studies [36,37], and only its main features are presented herein. The governing equations and the corresponding source/exchange terms are listed in Table 3.

Table 2
Properties/parameters used for the ProCAST simulation

Properties/parameters	Symbol *	Unit	Value	Refs
Thermophysical properties				
Density of superalloy	ρ_A	kg·m^{-3}	7646.0	[33]
Density of ceramic core	ρ_C	kg·m^{-3}	2320.0	-
Density of shell mold	ρ_M	kg·m^{-3}	3970.0	-
Initial liquidus of superalloy	T_L	K	1688.0	-
Eutectic temperature of superalloy	T_{eut}	K	1627.0	-
Thermal conductivity of superalloy	k_A	W·m^{-1}·K^{-1}	33.5 (l), 24.6 (s)	[33, 34]
Thermal conductivity of ceramic core	k_C	W·m^{-1}·K^{-1}	Fig. 3(a)	-
Thermal conductivity of shell mold	k_M	W·m^{-1}·K^{-1}	Fig. 3(a)	-
Specific heat of the superalloy	c_p	J·kg^{-1}·K^{-1}	575.0	[22, 33]
Latent heat of fusion of the superalloy	Δh_f	J·kg^{-1}	2.4×10^5	[22, 35]
Specific heat of the ceramic core	$c_{p,C}$	J·kg^{-1}·K^{-1}	Fig. 3(b)	-
Specific heat of the shell mold	$c_{p,M}$	J·kg^{-1}·K^{-1}	Fig. 3(b)	-
Initial/Boundary conditions				
Initial temperature for superalloy, mold, core	$T_{0,A}$, $T_{0,M}$, $T_{0,C}$	K	1773.0	-
Initial temperature for chill plate	$T_{0, Chill}$	K	303.0	-
Baffle emissivity	ε_{Baffle}	-	0.6	
Shell mold emissivity	ε_M	-	0.5	
Heating/Cooling wall emissivity	ε_{Wall}	-	0.6	
Heating wall	-	K	1773.0	
Cooling wall	-	K	353.0	
Withdrawal velocity	v	mm/min	1.5	
Interface heat transfer coefficients (HTC)				
Superalloy–Ceramic core	$h_{A\text{-}C}$	W·m^{-2}·K^{-1}	Fig. 3(c)	
Superalloy–Shell mold	$h_{A\text{-}M}$	W·m^{-2}·K^{-1}	Fig. 3(c)	
Ceramic core–Shell mold	$h_{C\text{-}M}$	W·m^{-2}·K^{-1}	1000.0	
Superalloy–Copper chill plate	$h_{C\text{-}B}$	W·m^{-2}·K^{-1}	5000.0	
Shell mold–Copper chill plate	$h_{M\text{-}B}$	W·m^{-2}·K^{-1}	20.0	
Numerical parameters				
Mesh size	Δx	mm	0.2–2.0	
Maximum time-step	Δt	s	5.0	

* Subscripts, 'A', 'C' and 'M' are used to indicate the material regions, 'superalloy', 'ceramic core', and 'shell mould', respectively. The subscript '0' indicates the initial condition.

(1) Only two phases (liquid melt and solid) were included, as shown in Fig. 4(a). The solid phase represents columnar dendrites.
(2) The volume fractions (f_ℓ, f_s), temperature (T_ℓ, T_s), velocity field of the melt ($\vec{u}_\ell$), and volume-averaged concentrations in both

Table 3

Governing equations of the two-phase columnar solidification model.

Governing equations	Symbols*
1. Mass conservations: $$\frac{\partial}{\partial t}(f_\ell \rho_\ell) + \nabla \cdot (f_\ell \rho_\ell \vec{u}_\ell) = -M_{\ell s} \quad (7)$$ $$\frac{\partial}{\partial t}(f_s \rho_s) = M_{\ell s} \quad (8)$$ with $f_\ell + f_s = 1$ $$M_{\ell s} = v_{R_s} \cdot (\pi d_s / \lambda_1^2) \cdot \rho_s \cdot f_\ell \quad (9)$$ $$v_{R_s} = \frac{D_\ell}{d_s/2} \frac{(c_\ell^* - c_\ell)}{(c_\ell^* - c_s^*)} \ln^{-1}\left(\frac{R_{f,s}}{d_s/2}\right) \quad (10)$$	f_ℓ, f_s, volume fraction [-] ρ_ℓ, ρ_s, density [kg·m^{-3}] $\vec{u}_\ell$, liquid velocity [m·s^{-1}] $M_{\ell s}$, net mass transfer rate [kg·m^{-3}·s^{-1}] v_{R_s}, dendrite growth speed [m·s^{-1}] d_s, dendrite trunk diameter [m] D_ℓ, diffusion coefficient [m^2·s^{-1}] c_ℓ, specie concentration [-] c_ℓ^*, c_s^*, equilibrium concentration at interface [-] $R_{f,s}$, maximum radius of dendrite trunk [m] λ_1, primary dendrite arm spacing [m] $\bar{\bar{\tau}}_\ell$, stress-strain tensors [kg·m^{-1}·s^{-1}] P, pressure [N·m^{-2}]
2. Momentum conservations: $$\frac{\partial}{\partial t}(f_\ell \rho_\ell \vec{u}_\ell) + \nabla \cdot (f_\ell \rho_\ell \vec{u}_\ell \otimes \vec{u}_\ell) = -f_\ell \nabla p + \nabla \cdot \bar{\bar{\tau}}_\ell + f_\ell \rho_\ell \vec{g}'_\ell - \vec{U}_{\ell s} \quad (11)$$ $$\vec{g}'_\ell = \frac{\rho_\ell^b(T, c_\ell) - \rho_\ell^{ref}}{\rho_\ell^{ref}}\vec{g} \quad (12)$$ $$\rho_\ell^b(T, c_\ell) = \rho_\ell^{ref} \cdot (1 + \beta_T \cdot (T^{ref} - T_\ell) + \beta_c \cdot (c^{ref} - c_\ell)) \quad (13)$$ $$\vec{U}_{\ell s} = \vec{U}_{\ell s}^p + \vec{U}_{\ell s}^d \quad (14)$$ $$\vec{U}_{\ell s}^p = \begin{cases} \vec{u}_\ell \cdot M_{\ell s} & \text{solidification} \\ \vec{u}_s \cdot M_{\ell s} & \text{remelting} \end{cases} \quad (15)$$ $$\vec{U}_{\ell s}^d = \frac{f_\ell^2 \cdot \mu_\ell}{K} \cdot \vec{u}_\ell \quad (16)$$ $$K = 6 \times 10^{-4} \cdot \lambda_1^2 \cdot \frac{f_\ell^3}{(1 - f_\ell)^2} \quad (17)$$	$\vec{g}, \vec{g}'_\ell$, gravity and deduced gravity [m·s^{-2}] ρ_ℓ^b, density for buoyancy force [kg·m^{-3}] ρ_ℓ^{ref}, reference density [kg·m^{-3}] T^{ref}, reference temperature [K] c^{ref}, reference concentration [-] β_T, thermal expansion coefficient [K^{-1}] β_c, solutal expansion coefficient [wt.%$^{-1}$] $U_{\ell s}$, mom. exchange rate [kg·m^{-2}·s^{-1}] $\vec{U}_{\ell s}^p$, mom. Exchange due to phase change [kg·m^{-2}·s^{-2}] $\vec{U}_{\ell s}^d$, mom. exchange due to drag force [kg·m^{-2}·s^{-2}] K, permeability [m^2] c_s, specie concentration [-] D_s, diffusion coefficient [m^2·s^{-1}] $C_{\ell s}$, species exchange rate [kg·m^{-3}·s^{-1}] k, solute partition coefficient [-]
3. Species conservations: $$\frac{\partial}{\partial t}(f_\ell \rho_\ell c_\ell) + \nabla \cdot (f_\ell \rho_\ell \vec{u}_\ell c_\ell) = \nabla \cdot (f_\ell \rho_\ell D_\ell \nabla c_\ell) - C_{\ell s} \quad (18)$$ $$\frac{\partial}{\partial t}(f_s \rho_s c_s) = \nabla \cdot (f_s \rho_s D_s \nabla c_s) + C_{\ell s} \quad (19)$$ $$C_{\ell s} = \begin{cases} k \cdot c_\ell^* \cdot M_{\ell s} & \text{solidification} \\ c_s \cdot M_{\ell s} & \text{remelting} \end{cases} \quad (20)$$	
4. Enthalpy conservations: $$\frac{\partial}{\partial t}(f_\ell \rho_\ell h_\ell) + \nabla \cdot (f_\ell \rho_\ell \vec{u}_\ell h_\ell) = \nabla \cdot (f_\ell k_\ell \nabla \cdot T_\ell) - Q_{\ell s}^p - Q_{\ell s}^d \quad (21)$$ $$\frac{\partial}{\partial t}(f_s \rho_s h_s) = \nabla \cdot (f_s k_s \nabla \cdot T_s) + Q_{\ell s}^p + Q_{\ell s}^d \quad (22)$$ $$\begin{cases} Q_{\ell s}^p = (h_\ell - h_s) \cdot M_{\ell s} \text{ with} \\ h_\ell = \int_{T_{ref}}^{T_\ell} c_{p,\ell} dT + h_{\ell,ref} \text{ and } h_s = \int_{T_{ref}}^{T_s} c_{p,s} dT + h_{s,ref} \\ h_\ell - h_s = \Delta h_f \end{cases} \quad (23)$$ $$Q_{\ell s}^d = H^* \cdot (T_\ell - T_s) \quad (24)$$ where H^* infinitive (10^9 W•m^{-3}•K^{-1})	h_ℓ, h_s, enthalpy [J·kg^{-1}] $h_{\ell,ref}, h_{s,ref}$, reference enthalpy [J·kg^{-1}] Δh_f, latent heat of fusion [J·kg^{-1}] $c_{p,\ell} = c_{p,s}$, specific heat T_ℓ, T_s, temperature [K] k_ℓ, k_s, thermal conductivity [W·m^{-1}·K^{-1}] $Q_{\ell s}^p$, energy exchange due to phase change [J·m^{-3}·s^{-1}] $Q_{\ell s}^d$, energy exchange between phases [J·m^{-3}·s^{-1}] H^*, volume heat transfer coefficient [W·m^{-3}·K^{-1}]

* Subscripts ℓ and s indicate the liquid and solid phases.

liquid and solid (c_ℓ, c_s) were obtained by solving the mass, energy, momentum, and species conservation equations (Table 3).

(3) A simplified cylindrical morphology was assumed for columnar dendrite development. The columnar tip front depicted in Fig. 4 (c) was traced considering the kinetics of the Lipton–Glicksman–Kurz model [38]. Only the base of the TB was allowed to initiate columnar dendrites.

(4) Thermodynamic equilibrium was assumed to be valid at the solid–liquid interface. Diffusion of solutes around crystal dendrites determines the solidification rate. The concentration difference ($c_\ell^* - c_\ell$) between the averaged thermodynamic equilibrium concentration at the interface (c_ℓ^*) and the local volume-averaged concentration (c_ℓ) served as the driving force for solidification.

(5) The mushy zone (Fig. 4(a)–(b)) was regarded as a porous medium, wherein Darcy's law was used to compute the flow. The permeability of the mushy zone was calculated as a function of f_ℓ and primary dendrite arm spacing, λ_1.

(6) Thermo–solutal convection was modelled using the Boussinesq approach. The solidification shrinkage was not considered in this study.

(7) The multicomponent superalloy was considered to be a binary alloy with constant liquidus slopes (*m*) and solute partition coefficients (*k*). The equivalent solute concentration was calculated using Eq. (3) [39,40]

$$c_\ell^0 = \sum_{i=1}^{N} c_{\ell,i}^0, \quad (3)$$

where *N* denotes the number of solute elements. The equivalent liquidus slope *m*, the equivalent solute partition coefficient *k*, and the equivalent solute expansion coefficient β_c, could be evaluated using the same method according to Eqs. (4) and (6), respectively:

$$c_\ell^0 \cdot m = \sum_{i=1}^{N} m_i \cdot c_{\ell,i}^0 \quad (4)$$
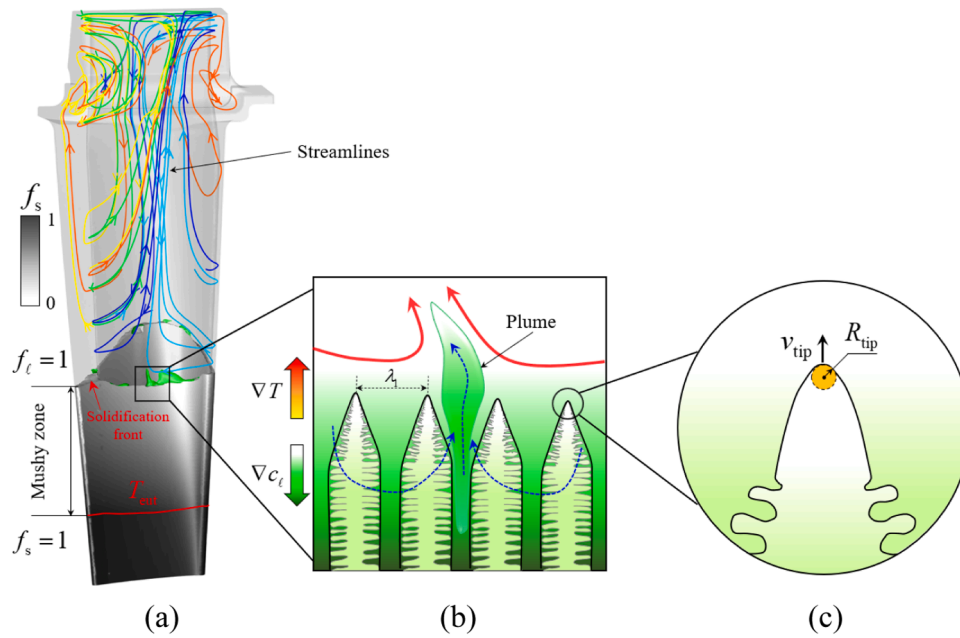
Fig. 4. Schematic of VA-based solidification model. (a) Flow pattern in the bulk liquid of the TB and marked mushy zone. (b) Liquid flow, development of plumes, and solidification of columnar dendrites near the solidification tip fronts. The thick red arrows denote the bulk flow, and the thin blue arrows denote the liquid flow in the mushy zone and in a plume. (c) Sketch of kinetic growth of the dendrite tip.

$$c_\ell^0 \cdot m \bigg/ k = \sum_{i=1}^{N} m_i \cdot c_{\ell,i}^0 \bigg/ k_i, \tag{5}$$

$$c_\ell^0 \cdot (1 - k) \bigg/ \beta_c = \sum_{i=1}^{N} c_{\ell,i}^0 \cdot (1 - k_i) \bigg/ \beta_{c,i} \tag{6}$$

(8) The macrosegregation index [7,12] indicates potential freckles which is calculated using $c_{\text{mix}}^{\text{index}} = (c_{\text{mix}} - c_0)/c_0 \times 100\%$, where $c_{\text{mix}} = (f_\ell \rho_\ell c_\ell + f_s \rho_s c_s)/(f_\ell \rho_\ell + f_s \rho_s)$ is the mixture concentration.

The calculation domain of the VA-based solidification model is restricted to the TB body. The same initial condition inside the TB as in the ProCAST calculation was used. For the flow calculation, the top surface was applied a free-slip boundary condition, while the remaining surfaces were specified as no-slip walls. The alloy was assumed to be incompressible with constant density and viscosity. The ProCAST-calculated surface T profiles served as Dirichlet boundary conditions for the flow-solidification simulations in the TB. The material properties and processing parameters are presented in Table 4.

An average mesh size of 0.35 mm (minimal size 0.2 mm, maximal size 0.45 mm) was utilised for the main body of the TB, and the entire TB was meshed into 421 627 cells. Two simulation scenarios are considered. In Case I, the liquid flow was not solved; however, the cooling and corresponding solidification were calculated. The objective of the first case was to calibrate the current coupling approach by comparing the computed thermal field. Case II involved calculating the blade solidification and its interaction with the liquid flow. The onset and evolution of the freckles and eutectic accumulation were predicted. The currently employed VA-based solidification model was implemented in ANSYS FLUENT version 17.1. Case I executed for approximately eight days on a high-performance cluster (2.6 GHz and 28 cores), whereas Case II took approximately one month.

3.3. Coupling ProCAST with the VA-based solidification model

The 'digital twin' was achieved by coupling ProCAST with the VA-

Table 4
Material properties and processing parameters

Properties/parameters	Symbol	Units	Values	Refs
Thermophysical				
Liquid diffusion coefficient	D_ℓ	m$^2\cdot$s^{-1}	3.6×10^{-9}	[21]
Thermal expansion coefficient	β_T	K^{-1}	-1.16×10^{-4}	[21]
Solutal expansion coefficient	β_c	wt.%$^{-1}$	-0.228	Eq. (6) [21,24, 41]
Liquid viscosity	μ_ℓ	kg$\cdot$m$^{-1}\cdot$s^{-1}	4.9×10^{-3}	[21]
Thermodynamic				
Equivalent initial concentration	c_0	wt.%	35.09	Eq. (3) and Table 1
Equivalent liquidus slope	m	K (wt.%)$^{-1}$	-1.145	Eq. (4) [24,41]
Equivalent equilibrium partition coefficient	k	-	0.57	Eq. (5) [41–43]
Primary dendritic arm spacing	λ_1	μm	500.0	Exp. measurement
Melting point of the solvent	T_f	K	1728.0	-
Numerical parameters				
Mesh size	Δx	mm	0.2–0.45	-
Time-step	Δt	s	0.01	-

based solidification model. The temperatures calculated by ProCAST at predefined locations on the TB surface, as indicated by the blue surface points in Fig. 5(a)–(b), are output and stored as T–t cooling curves. A set of fitting equations (T–t curves) corresponding to all the selected blue surface points can be obtained. As depicted schematically in Fig. 5 (c), the blue points indicate the predefined locations for storing the T–t curves in ProCAST, whereas the red points represent the centroids of the grid cells utilised for flow and solidification simulation in the VA-based solidification model. The temperature at the red point was linearly interpolated from the stored T–t curves of the four blue points. Finally, the interpolated T–t temperature profiles were further programmed and
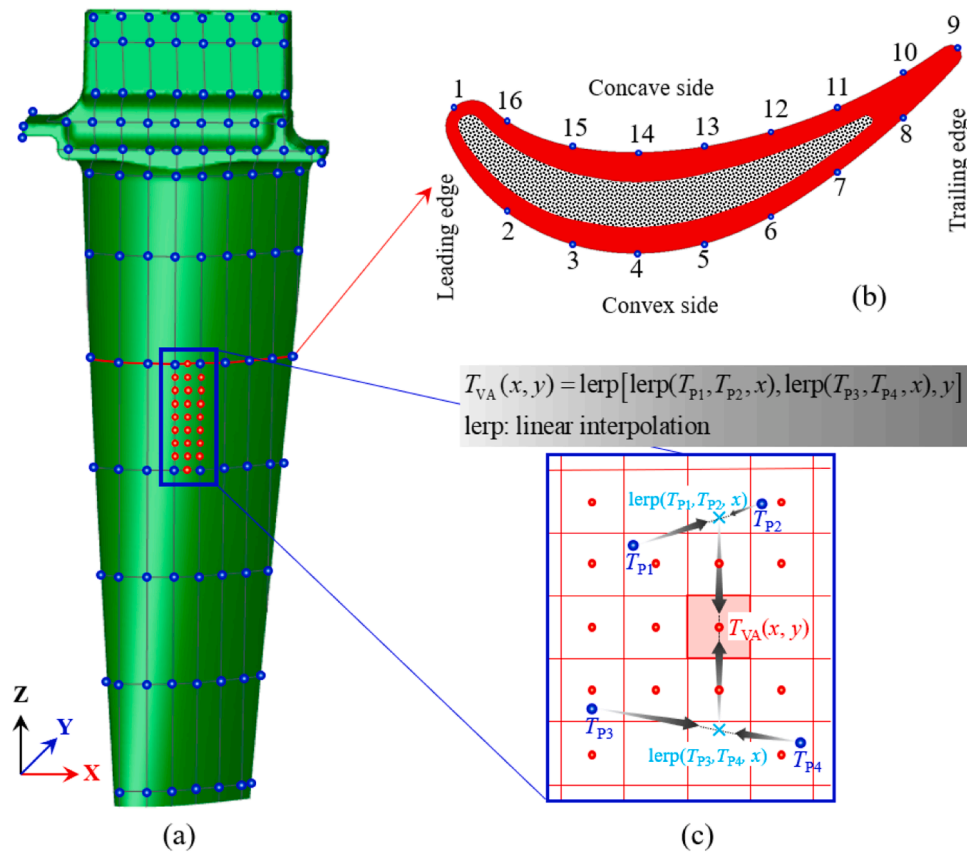
Fig. 5. Thermal coupling between ProCAST and VA-based solidification model. (a) Example of surface points for temperature extraction from ProCAST (blue points) and temperature interpolation for VA model (red points); (b) Surface points located at the cross-section of $Z = 0.18$ m; (c) Schematic figure to show the bilinear interpolation scheme between ProCAST and VA model.

used as thermal boundary conditions for the flow and solidification simulations.

4. Simulation results and comparison with the experiment

4.1. Temperature profiles

The calculated temperature field in the Bridgman furnace is illustrated in Fig. 6(a). Because of the shadowing effect in the furnace, the concave side of the TB facing the inducing wall was hotter than the convex side. The cooling curves at points 4 and 14 that are marked in Fig. 5(b), and the temperature difference between the two points are plotted in Fig. 6(d). The temperature difference between the two points varied between −21 K and 21 K. The temperature at Point 14 in the heating chamber was significantly higher than that at Point 4. At 7450 s after the two points passed the baffle, the difference in T had gradually decreased to zero. Eventually, the temperature of point 14 drops below that of point 4. This shadowing-effect-induced temperature difference led to an inclined solidification front. As depicted in Fig. 6(b), the solidification front on the convex side was 18 mm higher than that on the concave side. The isothermal surface for the eutectic reaction was also inclined, but its inclination (i.e. the height difference between the convex and concave sides) was significantly less than that of the solidification front. Fig. 6(c) illustrates the shape of the inclined solidification front determined using the VA solidification model, which exhibits the same shape as that calculated using ProCAST. At $t = 4500$ s, the temperature profiles calculated by ProCAST and the VA solidification model at the cross-section $Z = 0.18$ m are quantitatively compared in Fig. 6(e). Perfect replication of the temperature field in the VA solidification model demonstrates the reliability of the proposed coupling approach.

Notably, the temperature profiles and solidification front shapes of Case I (ignoring the flow) and Case II (considering the flow) using the VA solidification model were identical to the ProCAST simulation results. The analysis of the solidification sequence and the freckle formation in the remainder of this study is based on Case II.

4.2. Solidification sequence

Typical solidification results at 3300 s are depicted in Fig. 7. Fig. 7(a) displays the contour of the liquid concentration (c_ℓ) on the convex surface of the TB. In addition, the temperature (isotherms) on the convex surface, the positions of the solidification front ($f_s = 0.01$), and the end solidification (T_{eut}) on both the convex and concave sides are superimposed. Flow patterns in the bulk liquid region are represented by streamlines in Fig. 7(b). The liquid density (ρ_ℓ) of the convex surface is shown in Fig. 7(c). The as-developed plumes and segregation channels (as indicated by the isosurface $c_{mix}^{index} = 3\%$) and their liquid flow (coloured thick vectors) are depicted in Fig. 7(d). The temperature profiles and shape of the solidification front are bulged on the convex surface, which is identical to the results in Fig. 6(a) and (b). This type of temperature field led to the formation of two massive circulation loops in the bulk liquid region, as illustrated in Fig. 7(b). The relatively cold melt flows downward in the centre of the convex side. Near the solidification front, the melt flows to the concave side through the trailing and leading edges of the TB, and then flows upward in the centre of the concave side. Because of solute partitioning at the solid–liquid interface caused by solidification, the interdendritic c_ℓ is gradually enriched with increasing depth in the mushy zone, as shown in Fig. 7(a). The change in ρ_ℓ (owing to the combined thermal and solutal expansions) is depicted in Fig. 7(c). Above the solidification front, ρ_ℓ decreases with increasing height
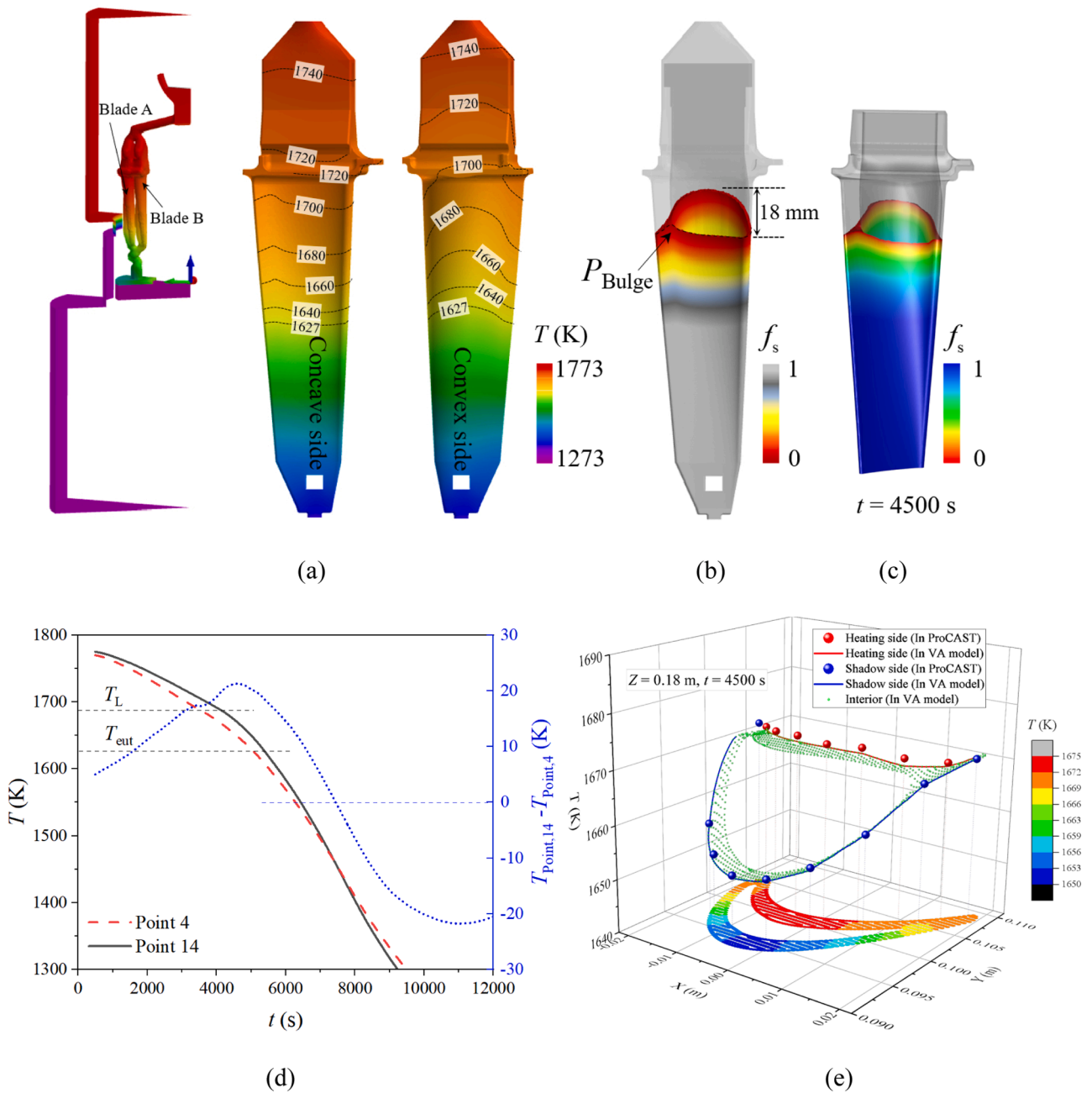
Fig. 6. Analysis of the temperature distribution on two surfaces of the TB and the solidification front in the TB at $t = 4500$ s. (a) Contour of the calculated temperature via ProCAST in the Bridgman furnace, and on the two sides of the TB. (b)–(c) Profiles of the solidification front calculated by ProCAST and VA solidification model. The local bulging of the solidification front on the concave side is marked by P_{Bulge} in (b). (d) Cooling curves at two points, 4 and 14 as marked in Fig. 5(b), and the temperature difference between the two points. (e) Comparison of the calculated temperature on the cross-section of $Z = 0.18$ m between ProCAST and VA solidification model.

because of the increased temperature; below the solidification front, ρ_ℓ decreases with depth owing to solute enrichment, and the maximum ρ_ℓ ($\rho_{\ell,max} = 7640$) occurs close to the solidification front. This density inversion renders the flow hydrodynamically unstable, i.e. a solute-rich liquid tends to rise to release its high gravitational potential energy. In Fig. 7(a), (c), and (d), the location (deep in the mushy zone) with high c_ℓ corresponds to the location with low ρ_ℓ, where the liquid has a strong tendency to rise. A few short plumes developed near the solidification front, but only two of these further evolved into segregation channels on the convex side. The vertical traces of the relatively high c_ℓ and low ρ_ℓ in the mushy zone (Fig. 7(a), (c)) indicate the as-developed segregation channels. As depicted in Fig. 7(d), the interdendritic solute-enriched

liquid rose along the segregation channels in the mushy zone. Once the interdendritic solute-enriched liquid flows out of the mushy zone, it is transported by strong bulk flow, i.e. the as-formed plumes are blown to the left or right ahead of the solidification front. According to the figure inset (horizontal section C–C) in Fig. 7(d), channel A is a weak internal channel, and channel B is a strong surface channel. Both channels are located on the convex side of the TB.

The solidification sequence of the TB and the evolution of the segregation channels are detailed in Fig. 8. They are presented in a view frame that retracts at the same rate as the TB (1.5 mm/min). The solidification front advanced to the bottom of the view frame at approximately 1910 s. Some plumes originate at the solidification front and
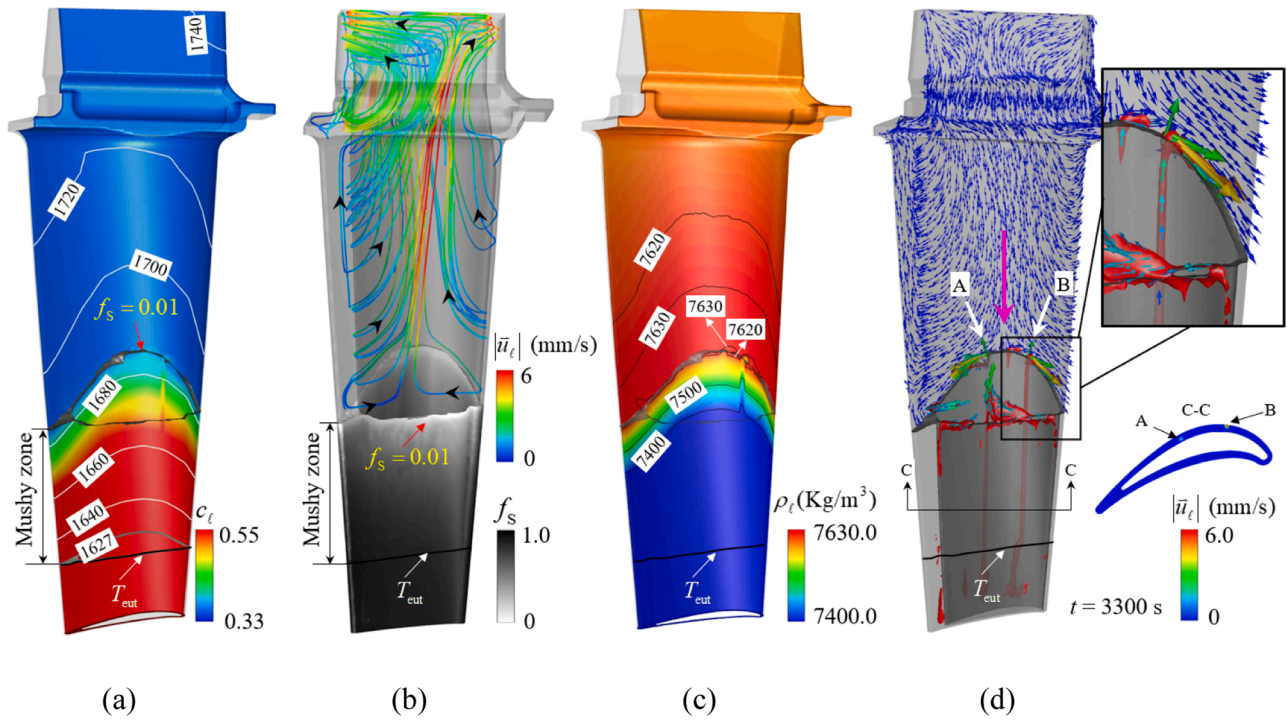
Fig. 7. Solidification results at 3300 s. (a) Contour of c_ℓ on the convex surface of the TB. The isotherms (K) on the convex surface, the solidification front ($f_s = 0.01$) and end solidification (T_{eut}) on both convex and concave surfaces are also superimposed. (b) Counter of f_s in the lower part overlaid by the streamlines to show the flow pattern in the bulk liquid. The color scale of the streamlines denotes the flow magnitude. (c) Counter and isolines of ρ_ℓ on the convex surface. (d) The red iso-surfaces ($c_{mix}^{index} = 3\%$) present the plumes (ahead of the solidification front) and segregation-channels (below the solidification front). The thin blue vectors on the convex surface indicate the flow direction in the bulk liquid region, and the thick colored vectors indicate the liquid velocity in the plumes/channels. One horizental section C–C is attached to display the positions of the formed segregation channels.
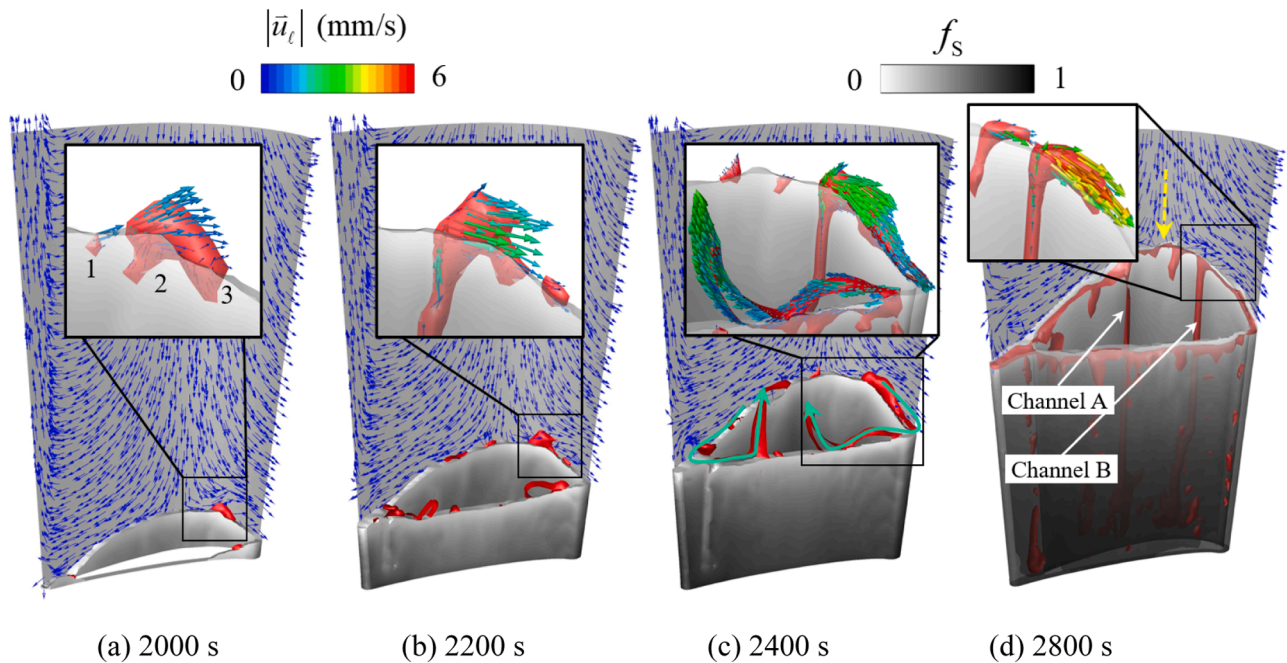
Fig. 8. Solidification sequence and evolution of the segregation channels. The gray contour depicts f_s and the profile of the solidification front. The plumes and the corresponding segregation channels are illustrated by red iso-surfaces $c_{mix}^{index} = 2\%$. The thin blue arrows on the convex surface denote the direction of bulk flow. The liquid flow in the plumes/channels are shown in the zoom-in views, in which the mushy zone is rendered transparent. In figure (d), the solid region is rendered transparent to display the channnels in the TB (plumes are not shown).

compete with one another. As depicted in Fig. 8(a), three newly formed plumes merged into one large plume on the convex surface. During the subsequent solidification process, from 2200 s (Fig. 8(b)) to 2400 s (Fig. 8(c)), the plume steadily grows stronger, eventually becoming a stable Channel B in Fig. 8(d). During this period, another segregation channel (Channel A) developed on the convex side. The position of the strongest downward flow on the convex side is indicated by the yellow dashed arrow in Fig. 8(d). Channel A is located to the left of the yellow arrow, whereas Channel B is located to the right. In Fig. 8(c), some plumes are observed to be 'bent' along the solidification front (due to the strong bulk flow). These plumes can transport solute-enriched melt from the convex side to the concave side and then flow upward again at the centre of the concave side.

4.3. Comparison of the calculated and experimentally observed freckles

The calculated freckles are compared to the experimentally observed ones in Fig. 9. On the convex side of the TB, the experimentally observed

freckles (I–IV) and several freckles above the platform were satisfactorily 'reproduced' numerically, as demonstrated in Fig. 9(a). The predicted freckle-V was not observed on the concave side, as shown in Fig. 9 (b). The discrepancy between the simulation and experiment with freckle-V is subsequently discussed. The freckles on the leading and trailing sides above the platform are compared in Fig. 9(c) and (d). The number and positions of experimentally observed freckles can also be accurately 'reproduced'. Excellent agreement between the simulation and experimental result was achieved.

4.4. Accumulation of eutectics

Additionally, the calculated distribution of the eutectic is compared to the experimental results shown in Fig. 10. Regarding Figs. 9(a) and 10 (a), it was discovered that freckles were associated with the accumulation of eutectics (f_{eut} = 40–80%). The top view of the TB is shown in Fig. 10(b). The eutectic accumulated not only in the freckles (e.g. dark circles/points), but also in the two designated corners A (f_{eut} = 68%) and

Fig. 9. Simulation–experiment comparison of the freckles in the as-solidified TB. Freckles appearing at different positions are numbered I–IX.
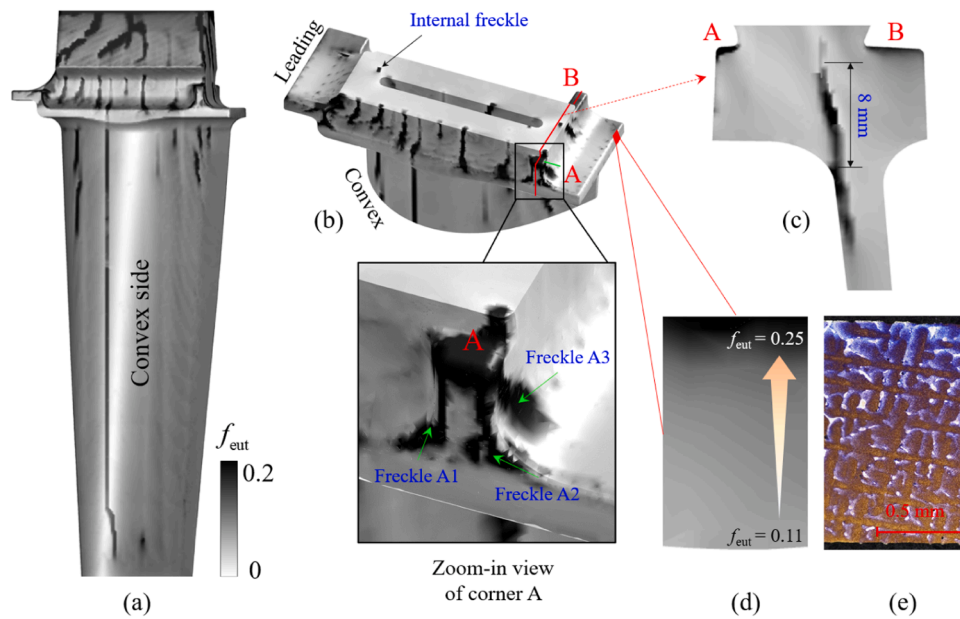
Fig. 10. The calculated distribution of f_{eut}. (a) Distribution of f_{eut} on the convex side of the TB. (b) Top view of the distribution of f_{eut}. A zoom-in view of corner A is presented in the inset. (c) Contour of f_{eut} on a vertical section along the red line as marked in (b). (d) Distribution of f_{eut} in a small rectangle marked in red colour in (b), and (e) the corresponding experimental observation (micrograph). In (e), the light area denotes the eutectic phase.

B ($f_{eut} = 27\%$). Observation of the internal dark circle indicates that freckles may form in the TB body, although they are more likely to appear on the TB surface. A vertical section was sliced along the red line, as illustrated in Fig. 10(b), and the f_{eut} distribution on this vertical section is shown in Fig. 10(c). In corners A and B, only a very thin layer of eutectic accumulated on the top. This is induced by the upward flow of the solute-enriched liquid in the plumes/channels during solidification, as theorised in [44]. The accumulation of the eutectic on the top

layer of corner A can also be understood by examining the magnified image in Fig. 10(b). Three short but distinct freckles (A1 to A3) emerged from the platform and converged at the top of corner A, indicating continuous solute transport to corner A during the solidification process. In Fig. 10(c), it is of considerable interest to note that the surface freckle continues to grow into the TB body following the expansion of the cross-section. It survived for a distance of eight millimetres before disappearing. The f_{eut} distribution on the platform, marked by the small red
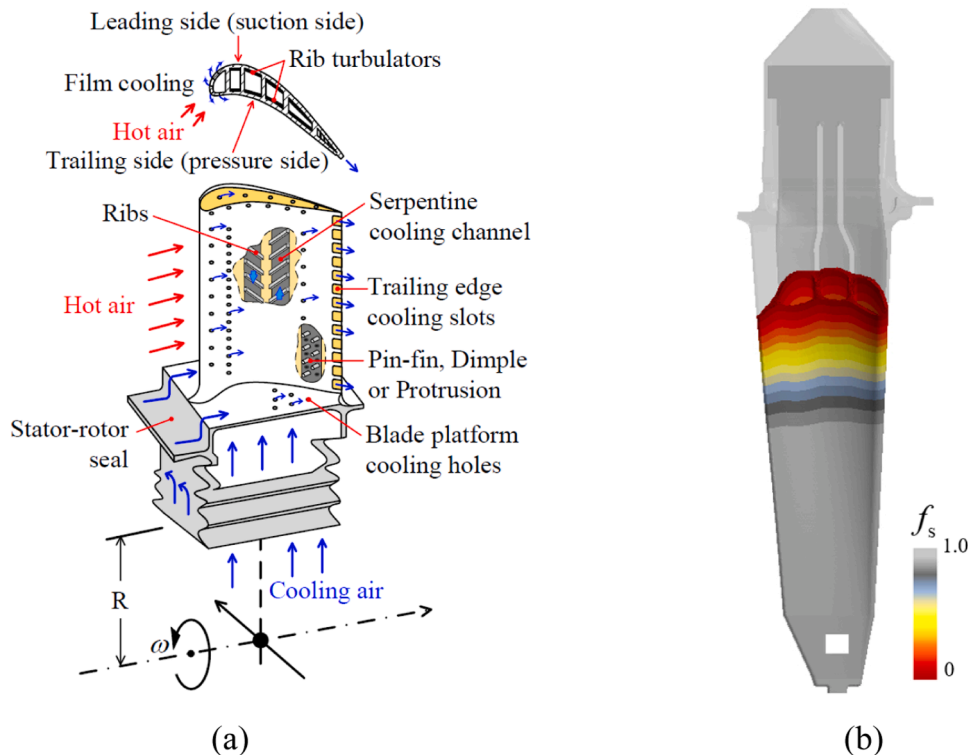
Fig. 11. (a) Schematic of internal structure with the cooling system (service) of an industrial TB [29]. (b) A simplified geometry with two internal fins connecting convex and concave blades is constructed.

rectangle in Fig. 10(b), was experimentally verified. A comparison with the simulation results is made in Fig. 10(d) and (e). Qualitatively, a satisfactory simulation–experiment agreement was obtained.

5. Discussion

5.1. Geometrical effect of the internal structure (fins) of the TB

As schematically depicted in Fig. 11(a) [29], the inner structure of an industrial TB is extremely complex. Ribs or fins are designed to increase the cooling inside the TB during its service in an aeroengine. The TB includes these ribs or fins that link the convex and concave blades. During the casting process, the effect of the internal structure of the TB on the temperature field and flow pattern, which further impacts freckle formation during solidification, is unknown. To examine the geometrical effects of the internal structure, a new simulation considering two thin fins, as depicted in Fig. 11(b), is performed, which connects the convex and concave sides of the TB

The thermal field for this new TB was calculated using ProCAST, as shown in Fig. 11(b). The newly calculated temperature on the outer surface of the TB was interpolated into the VA-based solidification model as thermal boundary conditions. Because the thermal conductivity of the superalloy (fins) is one order of magnitude larger than that of the ceramic core, the heat exchange between the convex and concave sides is expedited by the fins compared to the case without fins. Comparing Figs. 6(b) and 11(b), the inclination of the solidification

front (height difference between the convex and concave sides) is significantly reduced when the fins are considered. The fins also provide additional liquid flow pathways during solidification. As depicted in Fig. 12(a1), the liquid metal flows between the convex and concave sides not only via the trailing and leading edges but also through the fins. Several small vortices form on the convex side as a result of these additional paths, as shown in Fig. 12(b1). More plumes develop at the solidification front in Fig. 12(b1) than in the absence of fins (Fig. 12(b2)). The solute-enriched liquid flowed upwards in the plumes. The predicted segregation channels (potential freckles) are depicted in Fig. 12(c) and (d). The concave side is freckle-free for the case with fins in Fig. 12(c1), whereas one freckle is predicted for the case without fins, as shown in Fig. 12(c2). The case with fins (Fig. 12(c1)) is projected to have a channel on the inner surface of the convex side (facing the ceramic core), but the case without fins (Fig. 12(c2)) does not. In both cases, a relatively large vertical channel, associated with some short and inclined channels (branches), was observed on the outer surface of the convex side. Their respective positions and strengths are different. The liquid flow in the segregation channels is depicted in the inset of Fig. 12(d2). The upward flow in the large vertical channel was so strong that it sucked in the liquid from the surrounding area. Finally, the short and weak channels were inclined towards the large channel. The current simulation results verify the importance of the internal structure (fins) of the TB during the solidification process. Consequently, freckle formation is strongly related to this observation.

Manufacturing such a single-crystal TB with complete internal
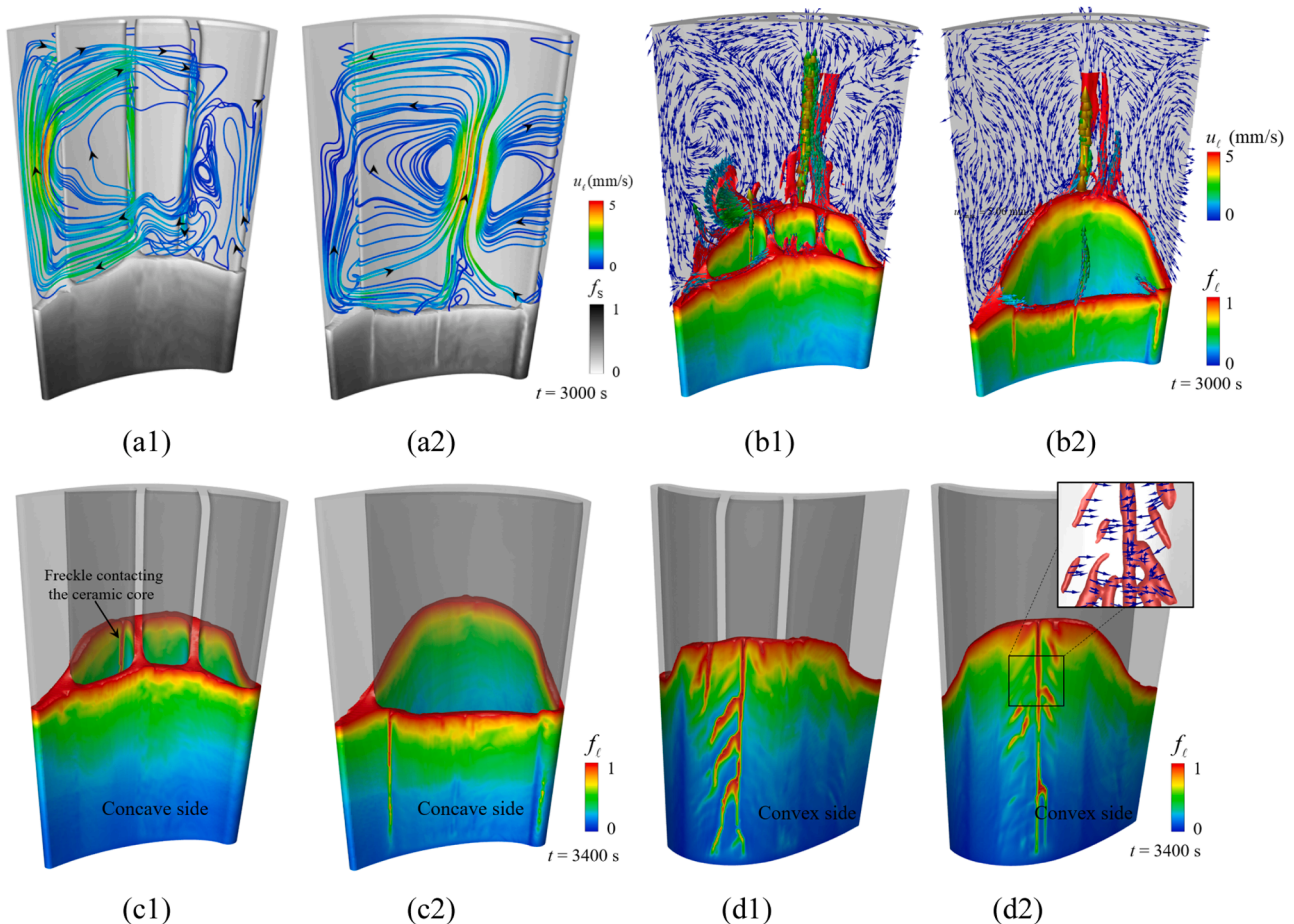
Fig. 12. Study of the effect of the internal structure (fins) on the formation of freckles. (a1)–(d1) are results of the case considering fins, and (a2)–(d2) are results of the case without fins. (a1)–(a2): contour of f_s overlaid by the liquid streamlines. (b1)–(b2): contour of f_ℓ. Iso-surfaces of $c_{\mathrm{mix}}^{\mathrm{index}} = 5\%$ are drawn for the plumes. The color vectors on the plumes present the local liquid velocity, and the blue vectors on the convex surface indicate the flow direction of the bulk liquid. (c1)–(c2) and (d1)–(d2): contour of f_ℓ to display the position and of potential freckles on the concave and convex sides of the TB. The inset zoom-in figure in (d2) presents the flow direction of the interdendritic liquid in the segregation channels ($c_{\mathrm{mix}}^{\mathrm{index}} = 5\%$).

structure is more of an art than a science, considering the complexity of the physical phenomena and their interplay during solidification. Despite extensive knowledge of the freckle formation mechanism, it remains impossible to empirically predict the freckle occurrence in such industrial TB. The digital twin of the solidification process would be the sole solution to this problem in the future. For commercial reasons, the actual TB with its inner structure detail is not presented here; however, the current study verifies the feasibility of the digital twin method. Currently, calculation time is an issue of concern. Consideration of all the structural details of the TB would necessitate more refined mesh size, i.e. more volume elements. However, this would not be a problem in the near future because the computational capacity doubles every 18 months (Moore's law).

5.2. The shadow effect of the furnace on the freckle formation

It is known that freckles are caused by thermo–solutal convection driven by density inversion in the mushy zone, but it is difficult to explain why more freckles developed on a particular location and/or a specific surface. The TB layout in the furnace is important, especially when they are produced in batches. Using the present instance as an example (Fig. 1), the temperature on the cooler (shadow) side of the TB facing the central rod is lower than that on the hot side. Consequently, the shape of the solidification front on the shadow side bulges significantly (Fig. 7(b)), so as do the ρ_ℓ distribution profiles (Fig. 7(c)). The solute-enriched interdendritic liquid at the peak of the bulged solidification front exhibited the highest potential energy to flow upward, making it the preferred position for the onset of plumes/freckles. On the hot side (facing the furnace wall), the solidification front is almost horizontal, as shown in Fig. 7(a). The isolines for c_ℓ and ρ_ℓ were also horizontal. The probability of forming plumes along the solidification front is identical everywhere. As depicted in Fig. 7(d), numerous tiny plumes attempt to start on the hot side. After their onset, these plumes are easily swept away by bulk convection, and none of them can form a persistent segregation channel. This phenomenon has been observed in a transparent cold model alloy 30NH₄Cl–H₂O [12].

5.3. Further improvement of the model

The digital twin of the TB was realised by coupling ProCAST with a VA-based multiphase solidification model. Further refinements to these models are discussed below.

(1) *Two-way full coupling between ProCAST and VA-based solidification model.* The liquid flow and flow-induced macrosegregation in the VA-based solidification model may alter the solidification path (i. e. the f_s–T relation), which should be fed back to the thermal calculation in ProCAST. Ideally, two-way coupling should be utilised for both calculations. Unfortunately, at the moment, this is not possible. The excellent simulation–experiment agreement observed for freckles and eutectic accumulation in the current study with one-way coupling suggests that two-way coupling is not necessary.

(2) *Mesh-size sensitivity.* Referring to the simulation–experiment agreement, the mesh size employed was acceptable. Using this mesh size, one simulation on a high-performance cluster (2.6 GHz and 28 cores) took around one month. As previously indicated, if all the structural elements of the TB are considered, the mesh size must be refined. However, this would not be a problem in the future, according to Moore's law. Additionally, further optimization of the calculation algorithm (e.g. adaptive time-step and dynamic adaption of the mesh) and improvement of the efficiency of the solidification code are also necessary to speed up the simulation in the future.

(3) *Direct simulation of stray grains.* The freckle was distinguished from the segregation channel by the stray grains. Terming

channels directly as freckles is not scientifically accurate. This causes quantitative error. It is true that the predicted channel is longer than the experimentally observed freckles shown in Fig. 9 (a). A further refinement employing a three-phase VA-based solidification model, that explicitly considers dendritic fragmentation [8,27], would distinguish freckles from segregation channels.

(4) *Multicomponent system.* The current multicomponent superalloy was treated as a pseudo-binary alloy [39,40]. On the basis of the good agreement between the simulation results and the experimental observations of the current work and other works [22,39, 40], this simplification seems to be acceptable. Referring to our previous work on the ternary alloy [45,46], the solidification path should be calculated properly by considering the multicomponent phase diagram, growth kinetics and the flow-induced macrosegregation. Thereby, further improvement by directly solving the solidification path of the superalloy is still needed.

A discrepancy was discovered between the simulation and experiment, as depicted by freckle-V in Fig. 9(b). This mismatch could be the result of both the numerical and experimental factors. The solidification front near the trailing edge (P_{Bulge} in Fig. 6(b)) bulges into the liquid phase because the superalloy has a higher thermal conductivity than the ceramic core. As discussed in Section 5.2, the bulged solidification front is the preferred position for the onset of the freckles. However, ignoring the liquid flow during the thermal calculation in ProCAST might overestimate this bulging, which could lead to the formation of freckle-V. Experimentally, the ceramic core was not ideally positioned. It was slightly off-centred towards the concave side, i.e. the convex side wall was slightly thicker than that of the concave side. Such experimental imperfections may cause a stronger flow on the convex side. If so, according to Fig. 7(b), the liquid flowing along the solidification front near the trailing edge may be intensified, which may suppress the formation of freckles at the P_{Bulge}. Such experimental imperfections should be avoided.

6. Conclusions

A novel method to 'digital-twin' the DS process of the industry TB was proposed by utilising a physics-based numerical model to quantitatively predict the solidification process. A two-step approach was adopted: the global thermal field in the Bridgeman furnace, including the casting system, was estimated using ProCAST, and then the flow and solidification inside the TB were simulated using a VA-based multiphase solidification model. The temperature profile on the TB surface calculated by ProCAST was interpolated as the thermal boundary condition for the VA-based solidification model. To prove this concept, an actual TB superalloy was cast in a Bridgman furnace and the as-solidified TB was inspected for freckles. An excellent simulation–experiment agreement regarding freckle formation and eutectic phase distribution was achieved. The proposed digital twin concept was verified to be feasible and reliable.

A numerical study was conducted on the effect of the inner structure (ribs or fins) of the TB on the DS process. The inner structure was discovered to play a crucial role in the heat–mass–momentum transfer during solidification, which strongly influenced freckle formation. Despite the established knowledge about the freckle formation mechanism, the occurrence of freckles in such an industrial TB with a complex inner structure is not empirically predictable. The digital twin of the solidification process may be the sole necessary solution for future TB production.

The favourable position for freckle formation on the convex side of the current TB is due to the shadowing effect of the Bridgman furnace, i. e. the temperature on the convex side (i.e. shadow side) of the TB facing the central rod (colder) is lower than that on the concave side. The temperature profiles and shape of the solidification front on the convex

side bulge significantly, so to the ρ_ℓ profiles (density inversion). The solute-enriched interdendritic liquid at the peak of the bulged solidification front exhibits the highest gravitational potential energy to flow upward, making it the preferred position for the onset of the plumes/freckles. On the hot side, the temperature profiles, shape of the solidification front, and profiles for ρ_ℓ are horizontal. The probability of forming plumes is equal everywhere along the solidification front. Once a plume forms, it is swept away by bulk convection, and no plume develops into a stable channel.

Declaration of Competing Interest

The authors declare that they have no known competing financial interests or personal relationships that could have appeared to influence the work reported in this paper.

Acknowledgement

References

[1] G.P. Sabol, R. Stickler, Microstructure of Nickel-Based Superalloys, Phys. Status Solidi. 35 (1969) 11–52, https://doi.org/10.1002/pssb.19690350102.

[2] F.I. Versnyder, M.E. Shank, The development of columnar grain and single crystal high temperature materials through directional solidification, Mater. Sci. Eng. 6 (1970) 213–247, https://doi.org/10.1016/0025-5416(70)90050-9.

[3] A.F. Giamei, B.H. Kear, On the nature of freckles in nickel base superalloys, Metall. Trans. 1 (1970) 2185–2192, https://doi.org/10.1007/BF02643434.

[4] D. Ma, Y. Zhao, W. Xu, L. Pi, Z. Li, Surface effect on eutectic structure distribution in single crystal superalloy castings, Acta Met. Sin. 57 (2021) 1539–1548, https://doi.org/10.11900/0412.1961.2020.00404.

[5] P. Auburtin, T. Wang, S.L. Cockcroft, A. Mitchell, Freckle formation and freckle criterion in superalloy castings, Metall. Mater. Trans. B. 31 (2000) 801–811, https://doi.org/10.1007/s11663-000-0117-9.

[6] D. Ma, Novel casting processes for single-crystal turbine blades of superalloys, Front. Mech. Eng. 13 (2018) 3–16, https://doi.org/10.1007/s11465-018-0475-0.

[7] J.R. Sarazin, A. Hellawell, Channel formation in Pb-Sn, Pb-Sb, and Pb-Sn-Sb alloy ingots and comparison with the system NH4Cl-H2O, Metall. Trans. A. 19 (1988) 1861–1871, https://doi.org/10.1007/BF02645156.

[8] A. Hellawell, J.R. Sarazin, R.S. Steube, Channel convection in partly solidified systems, Philos. Trans. - R. Soc. London, A. 345 (1993) 507–544, https://doi.org/10.1098/rsta.1993.0143.

[9] D. Ma, S. Liu, S.Z. Lu, Dendrite fragmentation and the effects of fluid flow in castings, Jom 49 (1997) 18–20, https://doi.org/10.1007/BF02914650.

[10] M. Ghods, M. Lauer, S.R. Upadhyay, R.N. Grugel, S.N. Tewari, D.R. Poirier, Spurious grain formation at cross-sectional expansion during directional solidification: influence of Thermosolutal convection, J. Mater. Eng. Perform. 27 (2018) 3122–3130, https://doi.org/10.1007/s11665-018-3364-0.

[11] T.M. Pollock, W.H. Murphy, The breakdown of single-crystal solidification in high refractory nickel-base alloys, Metall. Mater. Trans. A. 27 (1996) 1081–1094, https://doi.org/10.1007/BF02649777.

[12] S.M. Copley, A.F. Giamei, S.M. Johnson, M.F. Hornbecker, The origin of freckles in unidirectionally solidified castings, Metall. Trans. 1 (1970) 2193–2204, https://doi.org/10.1007/BF02643435.

[13] D. Han, W. Jiang, J. Xiao, K. Li, Y. Lu, L. Lou, Influence of geometric structure and feeding behavior of casting on freckle formation during directional solidification of a Ni-Based single-crystal superalloy, Cryst. Res. Technol. 56 (2021) 1–11, https://doi.org/10.1002/crat.202000197.

[14] D. Han, Q. Wu, A. Bührig-Polaczek, Some new observations on freckle formation in directionally solidified superalloy components, Metall. Mater. Trans. B. 43 (2012) 344–353, https://doi.org/10.1007/s11663-011-9608-0.

[15] D. Ma, A. Bührig-Polaczek, The geometrical effect on freckle formation in the directionally solidified superalloy CMSX-4, Metall. Mater. Trans. A. 45 (2014) 1435–1444, https://doi.org/10.1007/s11661-013-2088-x.

[16] D.X. Ma, Z.H. Dong, F. Wang, H.B. Dong, A phenomenological analysis of freckling in directional solidification of Ni-Base superalloy: the role of edge and curvature in casting components, Metall. Mater. Trans. A. 51 (2020) 88–92, https://doi.org/10.1007/s11661-019-05513-5.

[17] D. Ma, M. Mathes, B. Zhou, A. Bührig-Polaczek, Influence of crystal orientation on the freckle formation in directionally solidified superalloys, Adv. Mater. Res. 278 (2011) 114–119, https://doi.org/10.4028/www.scientific.net/AMR.278.114.

[18] T. Takaki, M. Ohno, T. Shimokawabe, T. Aoki, Two-dimensional phase-field simulations of dendrite competitive growth during the directional solidification of a binary alloy bicrystal, Acta Mater 81 (2014) 272–283, https://doi.org/10.1016/j.actamat.2014.08.035.

[19] L. Yuan, P.D. Lee, A new mechanism for freckle initiation based on microstructural level simulation, Acta Mater 60 (2012) 4917–4926, https://doi.org/10.1016/j.actamat.2012.04.043.

[20] N. Ren, C. Panwisawas, J. Li, M. Xia, H. Dong, J. Li, Solute enrichment induced dendritic fragmentation in directional solidification of nickel-based superalloys, Acta Mater 215 (2021), 117043, https://doi.org/10.1016/j.actamat.2021.117043.

[21] S.D. Felicelli, D.R. Poirier, J.C. Heinrich, Modeling freckle formation in three dimensions during solidification of multicomponent alloys, Metall. Mater. Trans. B. 29 (1998) 847–855, https://doi.org/10.1007/s11663-998-0144-5.

[22] N. Ren, J. Li, C. Panwisawas, M. Xia, H. Dong, J. Li, Thermal-solutal-fluid flow of channel segregation during directional solidification of single-crystal nickel-based superalloys, Acta Mater 206 (2021), 116620, https://doi.org/10.1016/j.actamat.2020.116620.

[23] M. Wu, M. Stefan-Kharicha, A. Kharicha, A. Ludwig, Flow-solidification interaction: a numerical study on solidification of NH4Cl –70 wt.%H2O solution in a water-cooled mould with a large sample thickness, Int. J. Heat Mass Transf. 164 (2021), 120566, https://doi.org/10.1016/j.ijheatmasstransfer.2020.120566.

[24] M.C. Schneider, J.P. Gu, C. Beckermann, W.J. Boettinger, U.R. Kattner, Modeling of micro- and macrosegregation and freckle formation in single-crystal nickel-base superalloy directional solidification, Metall. Mater. Trans. A. 28 (1997) 1517–1531, https://doi.org/10.1007/s11661-997-0214-3.

[25] N. Ren, J. Li, C. Panwisawas, M. Xia, H. Dong, J. Li, Insight into the sensitivities of freckles in the directional solidification of single-crystal turbine blades, J. Manuf. Process. 77 (2022) 219–228, https://doi.org/10.1016/j.jmapro.2022.03.019.

[26] C. Beckermann, J.P. Gu, W.J. Boettinger, Development of a freckle predictor via rayleigh number method for single-crystal nickel-base superalloy castings, Metall. Mater. Trans. A. 31 (2000) 2545–2557, https://doi.org/10.1007/s11661-000-0199-7.

[27] D. Han, W. Jiang, J. Xiao, K. Li, Y. Lu, W. Zheng, S. Zhang, L. Lou, Investigation on freckle formation and evolution of single-crystal nickel-based superalloy specimens with different thicknesses and abrupt cross-section changes, J. Alloys Compd. 805 (2019) 218–228, https://doi.org/10.1016/j.jallcom.2019.07.045.

[28] R. Schadt, I. Wagner, J. Preuhs, P.R. Sahm, New aspects of freckle formation during single crystal solidification of CMSX-4, Miner. Met. Mater. Soc. TMS (2000) 211–218, https://doi.org/10.7449/2000/superalloys_2000_211_218.

[29] N. Kaewchoothong, K. Maliwan, C. Nuntadusit, Numerical simulations on flow and heat transfer in ribbed two-pass square channels under rotational effects, IOP Conf. Ser. Mater. Sci. Eng. 243 (2017), 012004, https://doi.org/10.1088/1757-899X/243/1/012004.

[30] W. Xu, F. Wang, D. Ma, X. Zhu, D. Li, A. Bührig-Polaczek, Sliver defect formation in single crystal Ni-based superalloy castings, Mater. Des. (2020) 196, https://doi.org/10.1016/j.matdes.2020.109138.

[31] M.M. Franke, R.M. Hilbinger, A. Lohmüller, R.F. Singer, The effect of liquid metal cooling on thermal gradients in directional solidification of superalloys: thermal analysis, J. Mater. Process. Technol. 213 (2013) 2081–2088, https://doi.org/10.1016/j.jmatprotec.2013.06.001.

[32] https://myesi.esi-group.com/downloads/software-documentation/procast-2020.0-user-guide-visual-cast-16.0-users-guide-online, (n.d.).

[33] D. Szeliga, Effect of processing parameters and shape of blade on the solidification of single-crystal CMSX-4 Ni-based superalloy, Metall. Mater. Trans. B. 49 (2018) 2550–2570, https://doi.org/10.1007/s11663-018-1347-z.

[34] J.D. Miller, T.M. Pollock, Process simulation for the directional solidification of a Tri-crystal ring segment via the bridgman and liquid-metal-cooling processes, Metall. Mater. Trans. A. 43 (2012) 2414–2425, https://doi.org/10.1007/s11661-012-1104-x.

[35] P.N. Quested, R.F. Brooks, L. Chapman, R. Morrell, Y. Youssef, K.C. Mills, Measurement and estimation of thermophysical properties of nickel based superalloys, Mater. Sci. Technol. 25 (2009) 154–162, https://doi.org/10.1179/174328408X361454.

[36] M. Wu, A. Ludwig, A. Kharicha, Volume-averaged modeling of multiphase flow phenomena during alloy solidification, Metals (Basel) 9 (2019) 229, https://doi.org/10.3390/met9020229.

[37] M. Wu, A. Ludwig, Using a three-phase deterministic model for the Columnar-to-Equiaxed transition, Metall. Mater. Trans. A. 38 (2007) 1465–1475, https://doi.org/10.1007/s11661-007-9175-9.

[38] J. Lipton, M.E. Glicksman, W. Kurz, Dendritic growth into undercooled alloy metals, Mater. Sci. Eng. 65 (1984) 57–63, https://doi.org/10.1016/0025-5416(84)90199-X.

[39] B.J. Yang, D.M. Stefanescu, J. Leon-Torres, Modeling of microstructural evolution with tracking of equiaxed grain movement for multicomponent Al-Si alloy, Metall. Mater. Trans. A. 32 (2001) 3065–3076, https://doi.org/10.1007/s11661-001-0181-z.

[40] Q.Y. Sun, Y. Ren, D.R. Liu, Numerical investigations of freckles in directionally solidified nickel-based superalloy casting with abrupt contraction in cross section, Results Phys 12 (2019) 1547–1558, https://doi.org/10.1016/j.rinp.2019.01.056.

[41] P.K. Sung, D.R. Poirier, S.D. Felicelli, Simulating the initiation of a channel during directional solidification of a superalloy, Metall. Trans. 32 (2001) 202–207, https://doi.org/10.1007/s11661-998-0333-5.

[42] R.A. Hobbs, S. Tin, C.M.F. Rae, A castability model based on elemental solid-liquid partitioning in advanced nickel-base single-crystal superalloys, Metall. Mater. Trans. 36 (2005) 2761–2773, https://doi.org/10.1007/s11661-005-0272-3.

[43] G. Matache, D.M. Stefanescu, C. Puscasu, E. Alexandrescu, Dendritic segregation and arm spacing in directionally solidified CMSX-4 superalloy, Int. J. Cast Met. Res. 29 (2016) 303–316, https://doi.org/10.1080/13640461.2016.1166726.

[44] H. Zhang, X. Liu, D. Ma, A. Ludwig, A. Kharicha, M. Wu, Potential eutectic accumulation in single crystal turbine blade due to geometry effect: a numerical study, IOP Conf. Ser. Mater. Sci. Eng. (2022).

[45] M. Wu, J. Li, A. Ludwig, A. Kharicha, Modeling diffusion-governed solidification of ternary alloys - Part 1: coupling solidification kinetics with thermodynamics, Comput. Mater. Sci. 79 (2013) 830–840, https://doi.org/10.1016/j.commatsci.2013.05.015.

[46] M. Wu, J. Li, A. Ludwig, A. Kharicha, Modeling diffusion-governed solidification of ternary alloys - Part 2: Macroscopic transport phenomena and macrosegregation, Comput. Mater. Sci. 92 (2014) 267–285, https://doi.org/10.1016/j.commatsci.2014.05.027.